Inversion of multi-component, multi-azimuth walkaway VSP data for the stiffness tensor

Pawan Dewangan* and Vladimir Grechka†

* *Center for Wave Phenomena, Department of Geophysics, Colorado School of Mines, Golden, CO 80401-1887*
† *Center for Wave Phenomena; now at Shell International Exploration and Production, Houston, TX 77001-0481*

ABSTRACT

Vertical seismic profiling (VSP), an established technique, can be used for estimating in-situ anisotropy that might provide valuable information for characterization of reservoir lithology, fractures, and fluids. The P-wave slowness components, conventionally measured in multi-azimuth, walkaway VSP surveys, allow one to reconstruct some portion of the corresponding slowness surface. A major limitation of this technique is that the P-wave slowness surface alone does not constrain a number of stiffness coefficients that may be crucial for inferring certain rock properties. Those stiffnesses can be obtained only by combining the measurements of P-waves with those of S (or PS) modes.

Here, we extend the idea of Horne and Leaney, who proved the feasibility of the joint inversion of the slowness and polarization vectors of P- and SV-waves for parameters of transversely isotropic media with a vertical symmetry axis (VTI symmetry). We show that there is no need to assume *a priori* VTI symmetry or any other specific type of anisotropy. Under the assumption that the receivers are placed in a locally homogeneous medium and given sufficient polar and azimuthal coverage of the data, the polarizations and slownesses of P and two split shear (S_1 and S_2) waves are sufficient for estimating all 21 local elastic stiffness coefficients c_{ij} that characterize the most general triclinic anisotropy. The inverted stiffnesses themselves indicate whether or not the data can be described by a higher-symmetry model.

We discuss three different scenarios for inverting noise-contaminated data. First, we assume that the layers are horizontal and laterally homogeneous so that the horizontal slownesses measured at the surface are preserved at the receiver locations. This leads to a linear inversion scheme for the elastic stiffness tensor $\boldsymbol{c}$. Second, if the S-wave horizontal slowness at the receiver location is unknown, the elastic tensor $\boldsymbol{c}$ can be estimated in a nonlinear fashion simultaneously with estimating the horizontal slowness components of S-waves. The third scenario includes the nonlinear inversion for $\boldsymbol{c}$ using only the vertical slowness components and the polarization vectors of P- and S-waves. We find the inversion to be stable and robust for the first and second scenarios. In contrast, errors in the obtained stiffnesses increase substantially when the horizontal slowness components of both P- and S-waves are unknown. We apply our methodology to a multi-azimuth, multi-component VSP data set acquired in the Vacuum Field, New Mexico, and show that the medium at the receiver level can be approximated by an azimuthally rotated orthorhombic model.

Introduction

Multi-azimuth walkaway vertical seismic profiling (VSP) can be used for measuring in-situ anisotropy. It is usually estimated from P-wave slowness surfaces $\boldsymbol{p}^{(P)}$ (e.g., Gaiser, 1990; Miller and Spencer, 1994) obtained by differentiating the traveltimes $t^{(P)}$ of the first arrivals with respect to the coordinates $\boldsymbol{x}$ of the surface sources as well as for the downhole geophones: $p_i^{(P)} = \partial t^{(P)}/\partial x_i$ ($i = 1, 2, 3$). Because of the acquisition geometry, the vertical slowness components $p_3^{(P)}$ are

obtained only at the geophone levels, whereas the horizontal components $p_1^{(P)}$ and $p_2^{(P)}$ are computed only at the Earth surface. To reconstruct the slowness surfaces at the geophone levels, one usually assumes lateral homogeneity of the overburden. Then, according to Snell's law, the horizontal slownesses $p_1^{(P)}$ and $p_2^{(P)}$ are preserved along any ray travelling from sources to downhole receivers. Although the presence of even mild lateral velocity variations is known to lead to noticeable distortions of the reconstructed slowness surfaces and, consequently, to substantial errors in the estimated anisotropic parameters (Gaiser, 1990; Sayers, 1997), Bakulin et al. (2000c) found a practical way of correcting the slownesses for lateral heterogeneity of the overburden. Still, P-wave slowness surfaces $\boldsymbol{p}^{(P)}$ are inherently insufficient for constraining several stiffness coefficients needed for describing certain rock properties. Combining P- and S-wave VSP data is necessary for a more comprehensive reservoir characterization.

In general, three-component geophones are required to record S-waves at oblique incidence and perform Alford-type rotation to separate the fast (S_1) and slow (S_2) shear-wave arrivals (Dellinger et al., 2001). In addition to the S_1- and S_2-wave traveltimes (which can be differentiated in the same manner as that for P-waves to obtain the slownesses), Alford rotation yields the polarization vectors $\boldsymbol{A}^{(S_1)}$ and $\boldsymbol{A}^{(S_2)}$ of the split shear waves. Since the polarizations are measured locally at the geophones, they can be used, along with the slownesses, for anisotropic parameter estimation. Horne and Leaney (2000) recognized this possibility and developed a procedure for joint inversion of P- and SV-wave VSP data for parameters of transversely isotropic media with a vertical symmetry axis (VTI). The VTI model, however, might be too simplistic for characterization of realistic reservoirs. For instance, the presence of vertical fractures is known to reduce the symmetry of effective media to orthorhombic, monoclinic, or even triclinic (Bakulin et al., 2000a, b; Grechka et al., 2001). Although some anisotropic coefficients can be estimated from reflection seismics, in general it is impossible to estimate all coefficients needed for reservoir characterization from surface data. Thus, it is important to examine whether or not multi-component, multi-azimuth, walkaway VSP data can be used to obtain parameters of lower-symmetry anisotropic media.

Here we show that all 21 stiffness coefficients can be found given a sufficient polar and azimuthal coverage of the data. Errors in their estimated values turn out to depend on the complexity of the overburden, which determines our ability to use the horizontal slowness components (measured at the surface) in the inversion. We consider three possible scenarios for the inversion of VSP data.

Scenario 1. The overburden is close to horizontally layered (Figure 1a), and lateral velocity variations of P- and S-waves are known, for instance, from surface seismics. The expense of shear-wave excitation can be avoided by obtaining the S modes from converted (PS) wave reflections. The possible influence of lateral velocity heterogeneity on the horizontal slowness components of P- and S-waves might be corrected applying the technique described by Bakulin et al.(2000c). With such a correction, local values of the slowness vectors $\boldsymbol{p}^{(P)}$, $\boldsymbol{p}^{(S_1)}$, and $\boldsymbol{p}^{(S_2)}$ and the polarizations $\boldsymbol{A}^{(P)}$, $\boldsymbol{A}^{(S_1)}$, and $\boldsymbol{A}^{(S_2)}$ of all three modes are available at the receiver locations and can be used to estimate the local elastic stiffness coefficients c_{ij}. This results in a linear inverse problem for the tensor $\boldsymbol{c}$ [see equations (1) below].

Scenario 2. It may happen that only conventional P-wave surface-source data were acquired, and the S-wave velocity distribution is unknown, or shear waves recorded by the downhole receivers correspond to PS-wave reflections from dipping interfaces (Figure 1b). In both cases, the horizontal slowness components $p_1^{(S_1)}$, $p_2^{(S_1)}$, and $p_1^{(S_2)}$, $p_2^{(S_2)}$ of S-waves are, in general, unknown at receiver locations. The tensor $\boldsymbol{c}$, however, can still be estimated by inverting the slownesses $\boldsymbol{p}^{(P)}$, $p_3^{(S_1)}$, and $p_3^{(S_2)}$ and the polarization vectors $\boldsymbol{A}^{(P)}$, $\boldsymbol{A}^{(S_1)}$, and $\boldsymbol{A}^{(S_2)}$ at the receiver locations. The inversion becomes nonlinear in this case.

Scenario 3. If the subsurface is so complicated that it is impossible to get acceptable estimates of the horizontal slownesses of either P- and S-waves at the receiver locations (Figure 1c), only the quantities $p_3^{(P)}$, $p_3^{(S_1)}$, $p_3^{(S_2)}$, and $\boldsymbol{A}^{(P)}$, $\boldsymbol{A}^{(S_1)}$, $\boldsymbol{A}^{(S_2)}$ constitute the input for estimating the tensor $\boldsymbol{c}$. The inversion problem is again nonlinear.

Below, we analyze these three inversion scenarios and apply the developed procedure to estimate the elastic stiffness tensor $\boldsymbol{c}$ for a multi-azimuth, multi-component VSP data set acquired in the Vacuum Field, New Mexico.

Analytic Background

The forward model for the inverse problem at hand is the Christoffel equation, which determines the polarization and slowness vectors of plane waves propagating in anisotropic media (e.g., Tsvankin, 2001):

$$F_i^{(Q)} \equiv c_{ijkl}\, p_j^{(Q)}\, p_k^{(Q)}\, A_l^{(Q)} - A_i^{(Q)} = 0\,, \qquad (1)$$

$$(Q = P,\, S_1,\, S_2;\; i, j, k, l = 1,\, 2,\, 3)\,.$$

As in typical notation, we require the polarization vectors $\boldsymbol{A}^{(Q)}$ to be normalized, $\left|\boldsymbol{A}^{(Q)}\right| = 1$, and assume summation over all repeated indexes from 1 to 3. The density-normalized stiffness tensor $\boldsymbol{c}$, as well as the vectors $\boldsymbol{p}$ and $\boldsymbol{A}$, are defined in a cartesian coordinate frame with the x_3-axis pointing downward. Our goal is to estimate the elastic stiffness tensor $\boldsymbol{c}$ by inverting equations (1).

Scenario 1. If the slowness and polarizations vectors ($\boldsymbol{p}^{(Q)}$ and $\boldsymbol{A}^{(Q)}$) of all three modes are measured

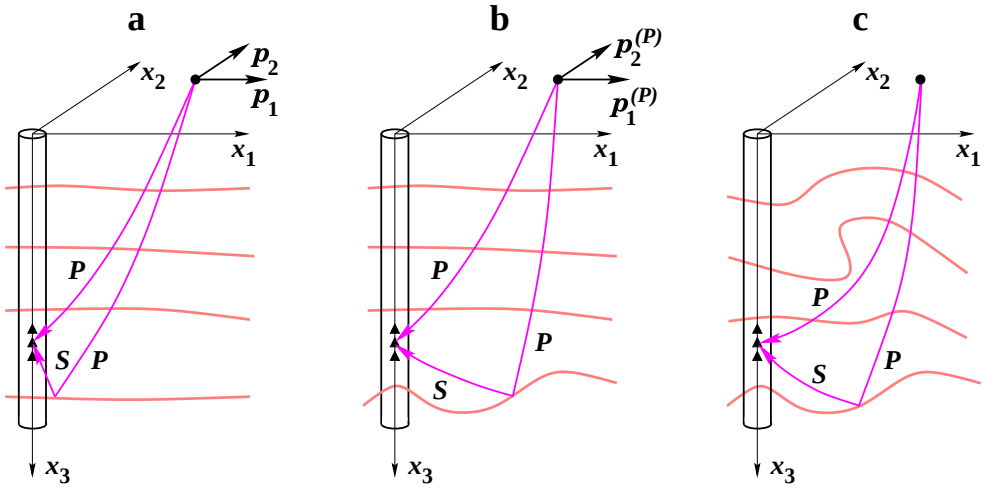

Figure 1. Three different scenarios of the inversion of multi-component VSP data corresponding to different levels of the complexity of the subsurface: (a) scenario 1, (b) scenario 2, and (c) scenario 3.

for N propagation directions, the only unknown in equations (1) is the tensor $\boldsymbol{c}$, under the assumption that the medium is locally homogeneous. Thus, the model and data vectors for scenario 1 are given by

$$\boldsymbol{m} = \boldsymbol{c}\,, \quad \boldsymbol{d} = \left\{\boldsymbol{p}_n^{(Q)},\, \boldsymbol{A}_n^{(Q)}\right\}, \tag{2}$$

$$(Q = P,\, S_1,\, S_2;\;\; n = 1,\, \ldots,\, N)\,.$$

Clearly, obtaining $\boldsymbol{c}$ from equations (1) is a linear inverse problem.

Scenario 2. When the horizontal slowness components of shear waves cannot be measured, the model and data vectors are

$$\boldsymbol{m} = \left\{\boldsymbol{c},\, p_{1,n}^{(S_1)},\, p_{2,n}^{(S_1)},\, p_{1,n}^{(S_2)},\, p_{2,n}^{(S_2)}\right\},$$

$$\boldsymbol{d} = \left\{\boldsymbol{p}_n^{(P)},\, p_{3,n}^{(S_1)},\, p_{3,n}^{(S_2)},\, \boldsymbol{A}_n^{(Q)}\right\}, \tag{3}$$

$$(Q = P,\, S_1,\, S_2;\;\; n = 1,\, \ldots,\, N)\,.$$

Since the slowness components $p_{i,n}^{(S_1)}$ and $p_{i,n}^{(S_2)}$ $(i = 1,\, 2)$ have to be estimated along with the components of the tensor $\boldsymbol{c}$, the inversion becomes nonlinear.

Scenario 3. Finally, when the horizontal slownesses of both P- and S-waves are unknown, we operate with the model and data vectors

$$\boldsymbol{m} = \left\{\boldsymbol{c},\, p_{1,n}^{(Q)},\, p_{2,n}^{(Q)}\right\}, \quad \boldsymbol{d} = \left\{p_{3,n}^{(Q)},\, \boldsymbol{A}_n^{(Q)}\right\}, \tag{4}$$

$$(Q = P,\, S_1,\, S_2;\;\; n = 1,\, \ldots,\, N)\,,$$

and the inversion procedure is again nonlinear.

To illustrate the increase in the number of unknowns from scenario 1 to scenario 3, let us assume that we have $N = 30$ spatial directions (data points) specified by particular azimuths and polar angles, where the polarizations and slownesses of all three modes are measured. We have three equations (1) for each mode, giving nine equations for each data point. Therefore, we have a total of $30 \times 9 = 270$ equations. Note that, for noise-free data, the number of independent equations reduces to $30 \times 6 = 180$ at the solution. This happens because one of three equations (1) can be expressed in terms of the other two due to the requirement of normalization $\left|\boldsymbol{A}^{(Q)}\right| = 1$. In scenario 1, the unknowns are the 21 in-situ stiffness coefficients c_{ij} for the most general triclinic anisotropy. In scenario 2, four unknown slowness components $p_1^{(S_1)}$, $p_2^{(S_1)}$, $p_1^{(S_2)}$, $p_2^{(S_2)}$ per each data point [equations (3)] have to be added, increasing the number of unknowns to $21 + 30 \times 4 = 141$. Similarly, in scenario 3 the total number of unknowns becomes $21 + 30 \times 6 = 201$ because the horizontal slownesses of all three modes are unknown [equations (4)]. The numbers of independent equations and unknowns are summarized in Table 1. Clearly, the inversion procedure in scenario 3 is under-determined at the correct solution.

Number of equations	Number of unknowns		
	Scenario 1	Scenario 2	Scenario 3
270 (180)	21	141	201

Table 1. Comparison of the numbers of equations and unknowns for a hypothetical VSP data set containing 30 points. Scenarios 1, 2, and 3 are illustrated in Figure 1.

Feasibility of Estimating Stiffness Coefficients from Walkaway VSP Data

In general, our ability to estimate a certain stiffness coefficient depends on the acquisition geometry. If, for instance, all ray trajectories in the data are close to the

vertical, the stiffness coefficients c_{11}, c_{12}, c_{22}, and c_{66}, which largely govern wave propagation near-horizontal directions, will be poorly constrained. The feasibility of estimating a particular stiffness coefficient can be evaluated by examining the Christoffel equation (1) written in the form

$$\boldsymbol{F}(\boldsymbol{m},\, \boldsymbol{d}(\boldsymbol{m})) = 0\,, \tag{5}$$

where $\boldsymbol{m}$ and $\boldsymbol{d}$ are the model and data vectors for the inversion scenarios given by equations (2)–(4). Then, the model and data perturbations relate as

$$\frac{\partial \boldsymbol{F}}{\partial \boldsymbol{m}}\,\Delta\boldsymbol{m} + \frac{\partial \boldsymbol{F}}{\partial \boldsymbol{d}}\,\Delta\boldsymbol{d} = 0\,. \tag{6}$$

The least-square estimate of data perturbation is given as,

$$\Delta\boldsymbol{d} = \boldsymbol{\mathcal{F}}\,\Delta\boldsymbol{m}\,, \tag{7}$$

where the matrix

$$\boldsymbol{\mathcal{F}} = -\left(\frac{\partial \boldsymbol{F}}{\partial \boldsymbol{d}}\right)^{\dagger} \frac{\partial \boldsymbol{F}}{\partial \boldsymbol{m}} \tag{8}$$

has the meaning of the Frechèt derivative matrix, and $\dagger$ denotes the pseudo-inverse.

Using the singular value decomposition (SVD) of the Frechèt matrix, we obtain

$$\boldsymbol{\mathcal{F}} = \boldsymbol{U}\boldsymbol{S}\boldsymbol{V}^{T}\,. \tag{9}$$

Here $\boldsymbol{U}$ and $\boldsymbol{V}$ are the eigenvector matrices in the data and model spaces, respectively, $\boldsymbol{S}$ is the diagonal matrix of the singular values, and T denotes transposition.

Figure 2 shows the singular values $\boldsymbol{s} \equiv \mathrm{diag}(\boldsymbol{S})$ of the matrix $\boldsymbol{\mathcal{F}}$ computed for inversion scenario 2 in a triclinic model. The spatial directions corresponding to 30 data points used in this example are given in the caption to Figure 2 and the length of the vector $\boldsymbol{s}$ is 141 (Table 1). As Figure 2 indicates, many of the singular values are small, suggesting that certain components of the model vector $\boldsymbol{m}$ [equations (3)] are poorly constrained by the data $\boldsymbol{d}$. To find out which parameters can be resolved, let us assume that the errors in our data are uncorrelated and have same covariance $Cov(\boldsymbol{d}) = \sigma^2(\boldsymbol{d}) = \mathrm{const}$ and calculate the standard deviation $\boldsymbol{\sigma}(\boldsymbol{m})$ of the model vector $\boldsymbol{m}$ assuming least square estimator (e.g., Press et al., 1987),

$$\sigma_j^2(\boldsymbol{m}) = \sum_{i=1}^{\dim(\boldsymbol{d})} \left(\frac{V_{ji}}{s_i}\right)^2 \sigma^2(\boldsymbol{d})\,, \quad j = 1,\, \ldots,\, \dim(\boldsymbol{m})\,. \tag{10}$$

where V_{ji} is the model eigenvector.

Figure 3 shows the standard deviation $\boldsymbol{\sigma}(\boldsymbol{m})$ in the units of $\boldsymbol{m}$, for unit pertubation in polarization and slowness vector. The typical values of slowness vector, for given range of angles, varies from 0.2 to 0.6 s/km. The unit pertubation of 1 s/km corresponds to 500% to 170% error in slownesses. For the same typical value of slowness, the percentage error in estimated horizontal slownesses of the shear waves ranges from 1000% to

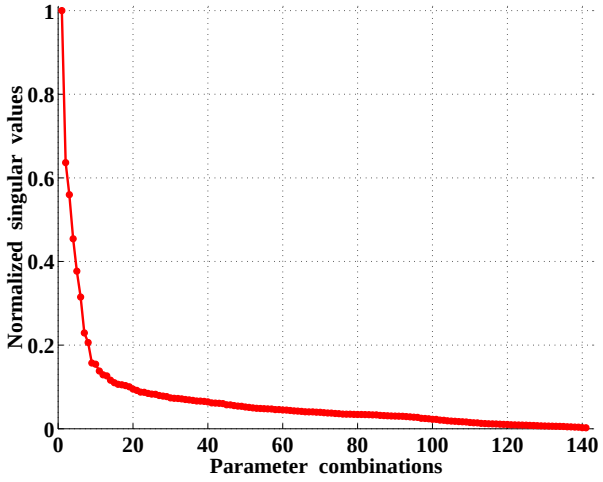

Figure 2. Singular values of the Frechèt matrix. The spatial directions used to generate data, at the receiver locations, are specified by five polar angles $\alpha^{(1)} = [13°,\, 26°,\, 39°,\, 52°,\, 65°]$ and six azimuths $\alpha^{(2)} = [0°,\, 30°,\, 60°,\, 90°,\, 120°,\, 150°]$. The model is described by the following density-normalized stiffness coefficients [in $\mathrm{km}^2/\mathrm{s}^2$]: $c_{11} = 4.00$, $c_{12} = 2.06$, $c_{13} = 2.10$, $c_{14} = -0.05$, $c_{15} = 0.01$, $c_{16} = -0.02$, $c_{22} = 3.83$, $c_{23} = 1.96$, $c_{24} = 0.12$, $c_{25} = -0.05$, $c_{26} = 0.13$, $c_{33} = 3.96$, $c_{34} = 0.11$, $c_{35} = 0.03$, $c_{36} = -0.09$, $c_{44} = 1.00$, $c_{45} = 0.11$, $c_{46} = -0.07$, $c_{55} = 0.88$, $c_{56} = 0.01$, $c_{66} = 1.11$.

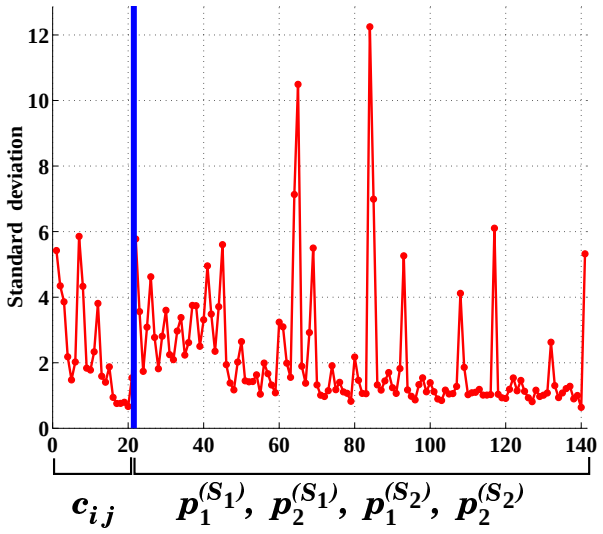

Figure 3. Standard deviations $\boldsymbol{\sigma}(\boldsymbol{m})$ computed using equation (10) for the model and data points given in the caption of Figure 2 assuming that the standard deviation of data errors is unity. The first 21 components of $\boldsymbol{\sigma}(\boldsymbol{m})$ correspond to the stiffness coefficients c_{ij}; the components from 22 to 141 represent the standard deviations in the horizontal slownesses of S-waves.

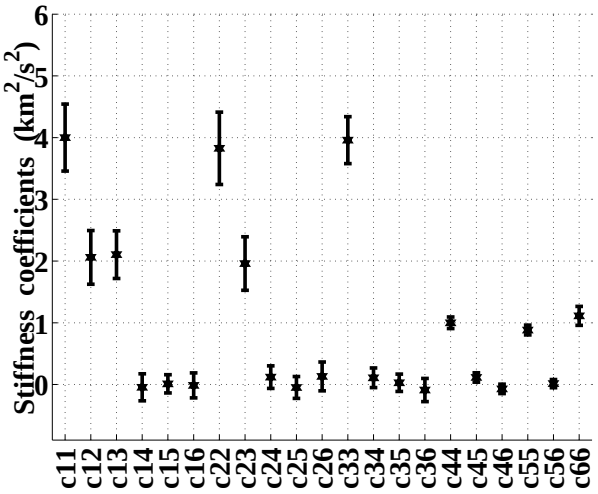

Figure 4. Confidence interval plot for the 21 elastic stiffness coefficients. Stars denote the c_{ij} given in the caption of Figure 2, bars represent ± 10% of the standard deviation shown in Figure 3.

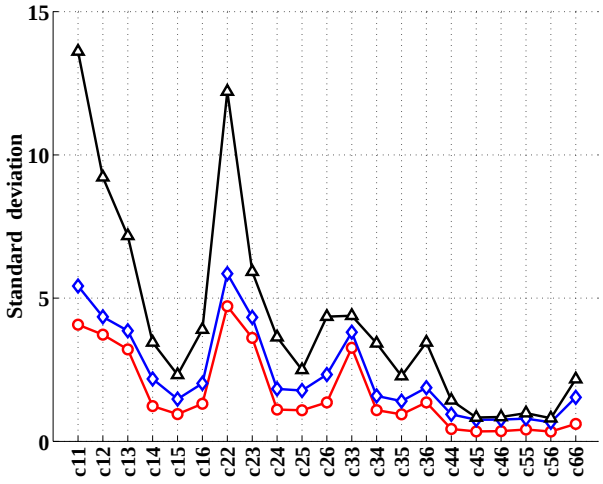

Figure 5. Comparison of the standard deviations $\boldsymbol{\sigma}(\boldsymbol{m})$ for inversion scenarios 1 (circles), 2 (diamonds), and 3 (triangles). As before, the data were computed at 30 spatial directions specified by polar angles $\alpha^{(1)} = [13°, 26°, 39°, 52°, 65°]$ and azimuths $\alpha^{(2)} = [0°, 30°, 60°, 90°, 120°, 150°]$.

160%. Thus, the error-amplification factor for the estimated horizontal slownesses is in general greater than unity. Similarly, the percentage error in estimated c_{ij} ranges from 150% for c_{11}, c_{22} and c_{66} to 100% for c_{33}, c_{44} and c_{55} indicating that the error-amplification factor for the stiffnesses c_{ij} is less than unity. Thus, the stiffnesses c_{ij} are relatively well constrained by our data $\boldsymbol{d}$. For smaller error in $\boldsymbol{d}$, the errors in $\boldsymbol{m}$ are scaled by the same amount [see equation (10)]. Figure 4 provides further insight into the feasibility of the inversion for the stiffness coefficients. Note that the computed errors for different components of the tensor $\boldsymbol{c}$ vary. The reason is the limited polar coverage of the data. Since the maximum of the polar angle $\alpha^{(1)}$ is 65° with the vertical (see the caption of Figure 2), the greatest error-amplification factors are associated with the stiffness coefficients c_{11}, c_{22} and c_{66} that determine the P and S-wave slownesses and polarizations in directions close to the horizontal. In contrast, the stiffnesses c_{33}, c_{44} and c_{55}, which govern P-wave and S-wave signatures near the vertical, are among the best constrained; their error-amplification factors are much smaller.

Figure 5 compares the standard deviations for the three different scenarios. As expected, the smallest errors in the estimated stiffnesses correspond to scenario 1, for which the number of unknowns is just 21 (Table 1). Interestingly, the errors in scenarios 1 and 2 are comparable, which suggests that knowing the horizontal slownesses of S-waves is not especially important for estimating the c_{ij}. On the other hand, in scenario 3 the standard deviations of some of the stiffness coefficients is substantially higher. Since in scenario 3 the number of unknowns is greater than the number of equations at the solution (Table 1), infinite errors (not shown) are associated with some horizontal slowness components that have to be found along with the stiffnesses.

We conclude this section by noting that the obtained results are based on the analysis of Frechèt derivative matrix, which represents the linearization of the truly nonlinear inverse problem in the vicinity of its solution. Next, we perform actual nonlinear inversion of synthetic noise-contaminated, multi-component VSP data and show that the above conclusions remain qualitatively valid.

Inversion Scheme and Numerical Results

For scenario 1, for which the horizontal slownesses of both P- and S-waves at the receiver location are known, the problem of obtaining the stiffnesses c_{ij} from equations (1) is linear. Its solution is given by

$$\boldsymbol{m} = \boldsymbol{\mathcal{F}}^{\dagger}\,\boldsymbol{d}\,, \tag{11}$$

where $\boldsymbol{\mathcal{F}}$ is the Frechèt matrix defined by equation (8).

In scenarios 2 and 3, when the inversion becomes nonlinear, we implemented the following procedure. First, given a trial stiffness tensor $\boldsymbol{c}$, we minimize $\boldsymbol{F}^2(\boldsymbol{c}, \boldsymbol{p}^{(Q)})$ [equation (1)] with respect to the horizontal slownesses $p_1^{(Q)}$ and $p_2^{(Q)}$ at each data point. Once estimates of the horizontal slownesses are obtained, we seek a minimum of the objective function

$$\Phi(\boldsymbol{c}) = \sum \boldsymbol{F}^2(\boldsymbol{c}, \boldsymbol{p}^{(Q)}) \tag{12}$$

with respect to $\boldsymbol{c}$. The summation here is performed over all data points, and the conjugate gradient method

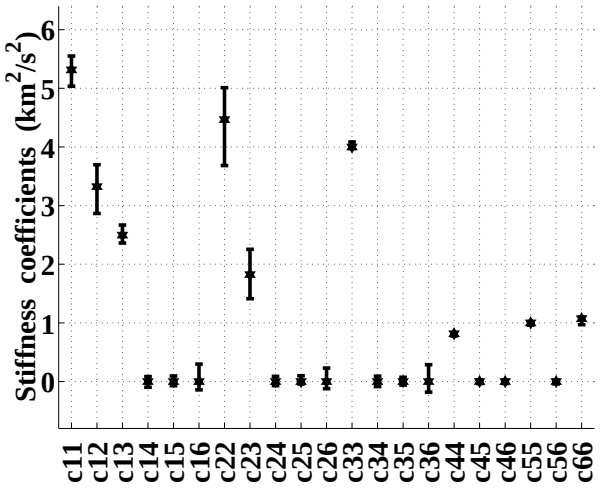

Figure 6. Results of linear inversion (scenario 1) of polarization and slowness vectors. Stars denote the exact values of the stiffness coefficients (corresponding to an orthorhombic model), bars represent ± one standard deviation in the estimated quantities. The data were computed at 24 directions specified by four polar angles $\alpha^{(1)} = [13°, 26°, 39°, 52°]$ and six azimuths $\alpha^{(2)} = [0°, 30°, 60°, 90°, 120°, 150°]$.

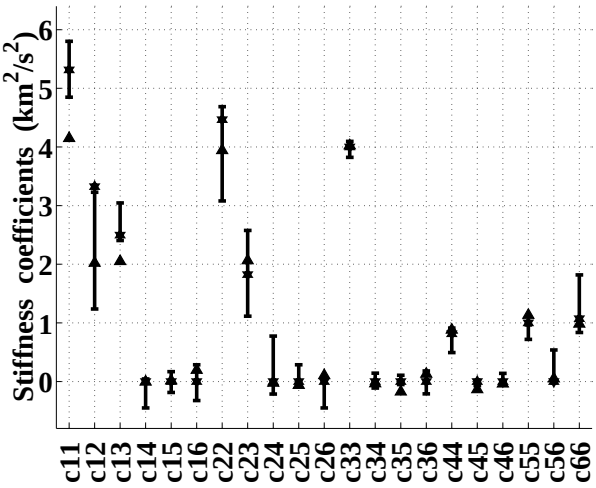

Figure 7. Inversion following scenario 2 for the same model; the data coverage is the same as in Figure 6; triangles represent the initial guess used for the inversion.

is used in both optimization steps. The main advantage of this inversion scheme is that it allows us to split the full parameter space, which includes both $\boldsymbol{c}$ and $\boldsymbol{p}^{(Q)}$, into a sequence of substantially smaller subspaces. As a result, we achieve both computational efficiency and rapid convergence.

To test the inversion algorithm, we computed the polarization and slowness vectors in an orthorhombic model. Then, the data were contaminated with Gaussian noise that had standard deviations 2% for the slownesses and 10° for the polarization vectors. The stiffnesses were estimated for different realizations of the noise. We did not use information about the symmetry of the model, so the data were inverted for triclinic media.

The results presented in Figure 6 (scenario 1) clearly indicate that all elements of the stiffness tensor that are strictly zero in the original orthorhombic medium are, indeed, small. Thus, knowing the symmetry of the model *a priori* is not needed for the inversion; the symmetry can be inferred from the results. The larger error bars for the computed stiffness coefficients c_{11}, c_{12}, and c_{22} as compared to those for c_{44} and c_{55} can be explained again by the limited polar coverage of the data (less than 52° with the vertical). Note that relative errors in the estimated stiffnesses are reasonably well predicted by the above analysis of Frechèt matrix (Figure 5).

When we follow scenario 2 to invert the stiffnesses from the same data [except for the slowness components $p_{1,n}^{(S_1)}$, $p_{2,n}^{(S_1)}$, $p_{1,n}^{(S_2)}$, and $p_{2,n}^{(S_2)}$ that now become a part of the model; compare equations (2) and (3)], we obtain less accurate results (Figure 7). Such loss of accuracy is predicted by the SVD analysis (compare the curves marked with circles and diamonds in Figure 5); more important, however, the estimates of several stiffness coefficients become biased. The primary reasons for the bias are the choice of starting models (shown as triangles in Figure 7) and the limited polar coverage of the data. Figure 7 indicates that the bias is more pronounced for poorly constrained stiffness coefficients such as c_{12} and c_{22}. This happens because of the chosen initial guess for the inversion (triangles in Figure 7), which was a weakly anisotropic triclinic model close to the isotropic one with Lamè constants $\mu = c_{44}$ and $\lambda = c_{33} - 2c_{44}$. Since the sensitivity of the objective function $\Phi(\boldsymbol{c})$ to the poorly constrained elements of the tensor $\boldsymbol{c}$ is low, the optimization algorithm tends to not change them, leaving their values close to the initial ones.

The error bars in Figure 7 are reduced when we increase the polar coverage of the data. Figure 8, where the maximum polar angle $\alpha^{(1)} = 65°$, indicates that the errors in the estimated stiffnesses become comparable to those in Figure 6, even though the horizontal slownesses of S-waves are now unknown. Also note that the increase in coverage somewhat reduces the bias in the estimated stiffnesses.

The inversion following scenario 3 (Figure 9) reveals a serious deterioration in the obtained estimates. Not only do the error bars generally increase compared to those in Figure 8, but the method also fails to constrain the stiffnesses c_{11}, c_{12}, c_{13} and c_{22}. Again, the reason for this can be seen in Figure 5. The standard deviations in c_{11}, c_{12}, c_{13} and c_{22} predicted by the SVD are so large that almost any values of those elastic coefficients fit the data. As a consequence, the estimates of

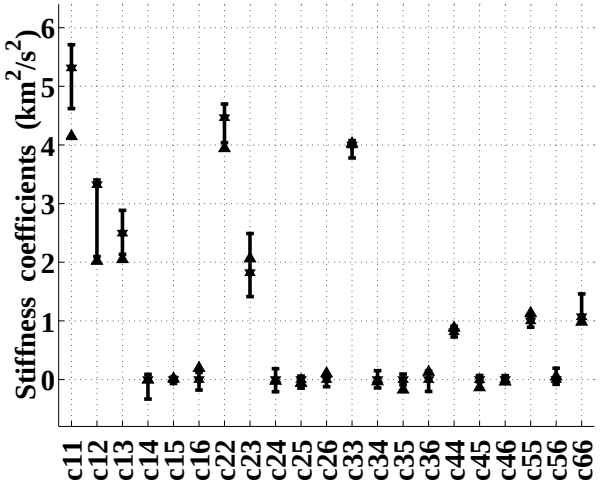

Figure 8. Same as Figure 7 but for the data generated at 30 directions given by five polar angles $\alpha^{(1)} = [13°, 26°, 39°, 52°, 65°]$ and six azimuths $\alpha^{(2)} = [0°, 30°, 60°, 90°, 120°, 150°]$.

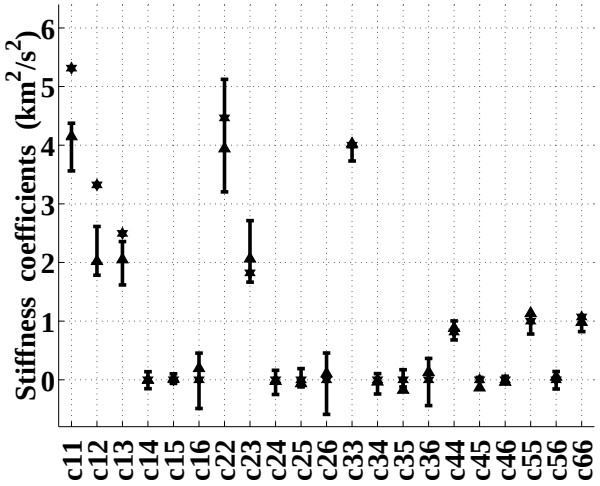

Figure 9. Inversion of the data with the coverage described in the caption of Figure 8 following scenario 3.

c_{11} and c_{12} in Figure 9 are biased, staying close to the corresponding initial guesses rather than converging to the correct values, and c_{22} has a large variability.

So far, we have avoided making any assumptions about the type of anisotropy of the model and attempted to estimate all 21 stiffness coefficients. Let us now reduce the number of unknown stiffnesses to nine by assuming the model to be orthorhombic with a known orientation of the symmetry planes. Figure 10 shows the inverted nonzero stiffness coefficients following scenario 2. Comparing Figures 8 and 10, we observe some decrease of the error bars. Although the symmetry is helpful for the inversion, however, Figures 8 and 10 indicate that it does not lead to significant improvement of the results.

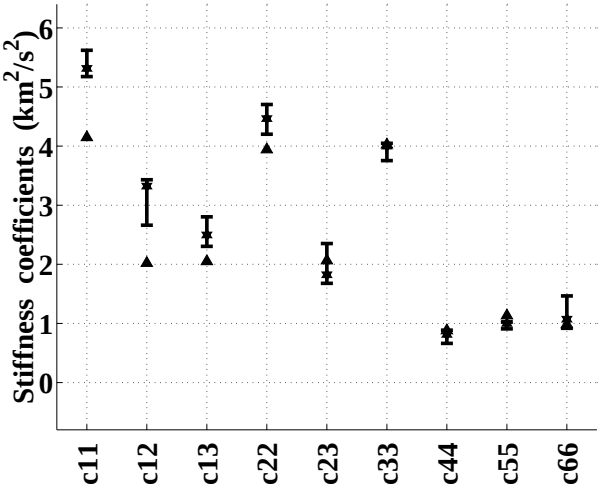

Figure 10. Same as Figure 8 but assuming that the model is orthorhombic with known orientation of the symmetry planes.

Field-data Example

Next, we apply our inversion scheme to a 3-D walkaway VSP data set acquired in the Vacuum field, Lea County, New Mexico. The data were recorded by a string of 10 three-component geophones placed in the vertical well VGWU 127 with a 15 m depth increment over the depth range 304.8 m to 439.8 m. Vertical and horizontal vibrators were used to excite P- and S-waves. The details of data acquisition can be found in Michaud (2001).

Estimation of polarization and slowness vectors

The initial data processing was performed by Michaud (2001). She applied the technique of DiSiena et al. (1984) to obtain the P-wave polarization vectors and used Alford (1986) rotation of the sources and receivers to separate two shear waves and find their polarization directions. The results for the receiver at depth 304.8 m are shown in Figures 11a–c.

The analysis of traveltimes $t^{(Q)}$ picked for P-, S_1-, and S_2-arrivals reveals the following: (i) traveltime minima $t_0^{(Q)}$ correspond to the borehole location for all receiver positions, (ii) traveltimes are symmetric with respect to the well. Based on these observations and to reduce the influence of random noise on traveltime picks, we have chosen to approximate the squared traveltimes $t^{(Q)}$ by a 2-D Taylor series

$$\left[t^{(Q)}(\boldsymbol{x})\right]^2 = \left[t_0^{(Q)}(x_3)\right]^2 + \sum_{j_1,\,j_2=1}^{2} a_{j_1 j_2}^{(Q)}(x_3) x_{j_1} x_{j_2}$$

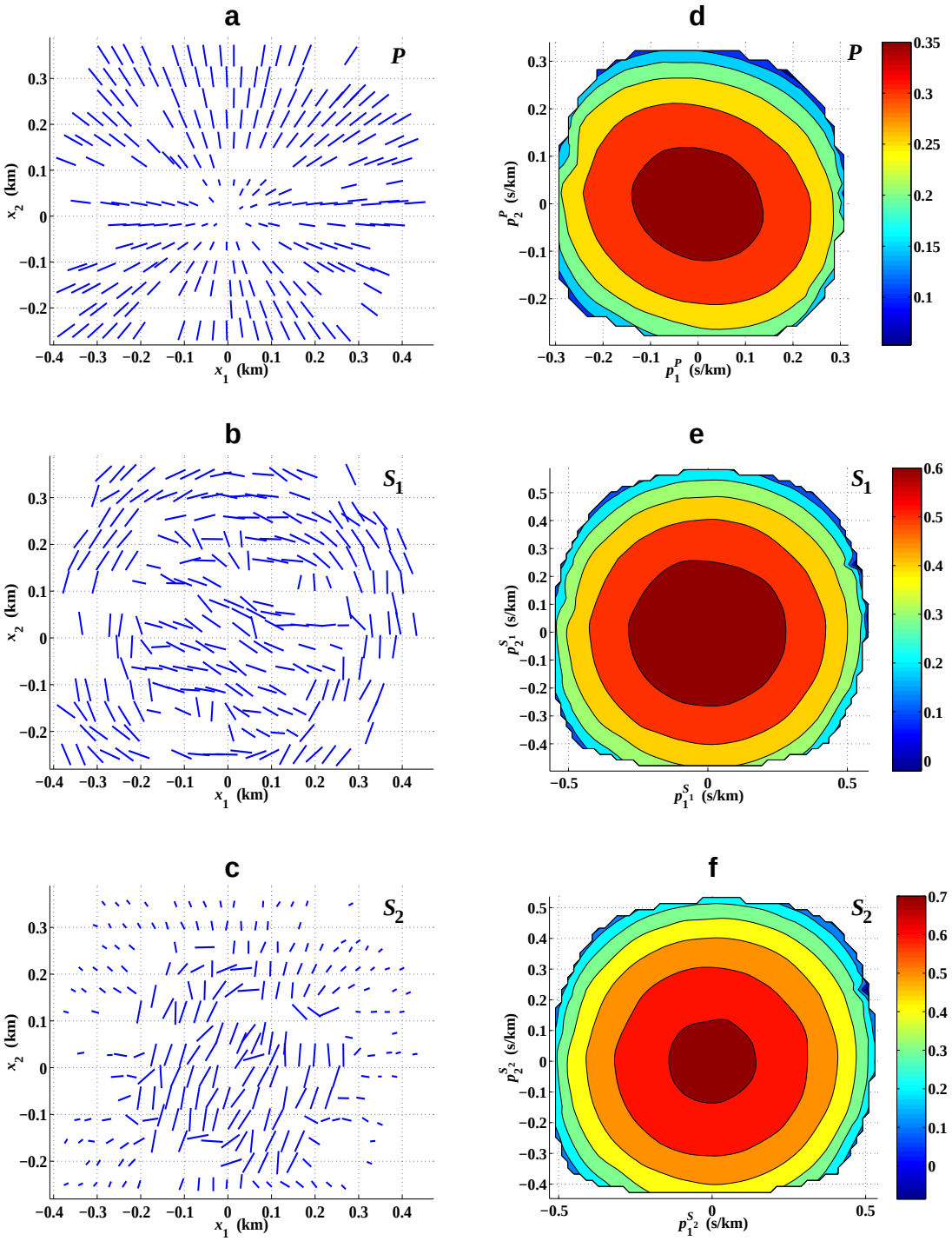

Figure 11. (a, b, c): Horizontal components of the polarization vectors $A_i^{(Q)}$ $(i = 1, 2)$; (d, e, f): vertical slowness components $p_3^{(Q)}(p_1^{(Q)}, p_2^{(Q)})$ of P-, S_1-, and S_2-waves for a receiver at depth 304.8 m in well VGWU 127. The well is located at $x_1 = x_2 = 0$.

$$+ \sum_{j_1,\,j_2,\,j_3,\,j_4=1}^{2} b^{(Q)}_{j_1 j_2 j_3 j_4}(x_3) x_{j_1} x_{j_2} x_{j_3} x_{j_4}\,, \quad (13)$$

$(Q = P,\, S_1,\, S_2)$.

Here the traveltimes $t^{(Q)}(\boldsymbol{x})$ are written in a cartesian coordinate frame $[x_1,\, x_2,\, x_3]$ with the origin at the borehole location and the axes x_1, x_2, and x_3 oriented in the east-west, north-south, and vertical directions, respectively; x_1 and x_2 denote the source coordinates, x_3 is the receiver depth. The coefficients $a^{(Q)}_{j_1 j_2}(x_3)$ and $b^{(Q)}_{j_1 j_2 j_3 j_4}(x_3)$ in equation (13) are symmetric with respect to interchange of any pair of their indexes. We find the quantities $\left[t^{(Q)}_0(x_3)\right]^2$, $a^{(Q)}_{j_1 j_2}(x_3)$, and $b_{j_1 j_2 j_3 j_4}(x_3)$ for all receiver levels x_3 using the least-squares method.

Next, we compute the slowness vectors according to their definition,

$$p^{(Q)}_i \equiv \frac{\partial t^{(Q)}}{\partial x_i}\,. \quad (14)$$

The result of this calculation for receiver at depth 304.8 is shown in Figures 11d–f. Note that the polar coverage of the data is extremely good. Since the polar angles reach 75°–80°, we might expect a comparable accuracy in the estimated stiffness coefficients that govern wave propagation both near-vertical and near-horizontal directions.

Inversion for stiffness coefficients

The studies done by Roche (1997) and the observed traveltime symmetry,

$$t^{(Q)}(x_1,\, x_2,\, x_3) = t^{(Q)}(-x_1,\, -x_2,\, x_3)\,, \quad (15)$$

indicate that the subsurface structure in the vicinity of well VGWU 127 is close to horizontally layered with almost no lateral velocity variation. This enables us to use the linear inversion strategy of scenario 1. We make no assumption about the medium symmetry and invert the data for a triclinic model. To obtain a suite of inversion results rather than a single model, we contaminate the smoothened polarizations and slownesses (such as those shown in Figure 11) with Gaussian noise. According to the estimates of Michaud (2001), the errors in the polarization and slowness vectors are 12° and 5%, respectively. We impose these values as the corresponding standard deviations.

It turns out that the inverted stiffness coefficients (Figure 12) are accurately described by an *azimuthally rotated* orthorhombic medium. Its local x_3'-axis has a tilt of 3° with respect to the horizontal $[x_1,\, x_2]$-plane and E-W azimuth. This tilt is statistically insignificant, so we can assume that the model has a horizontal symmetry plane. The local x_1'-axis points at 28° SE. The velocities (along the x_3'-axis) of the obtained orthorhombic model and its anisotropic coefficients (Tsvankin, 1997) are shown in Figure 13. Our

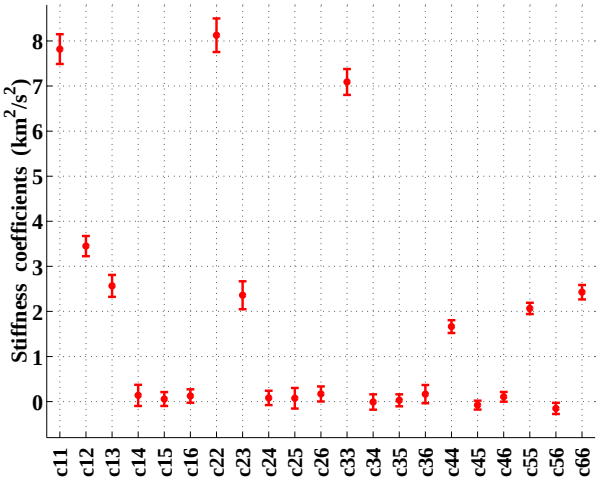

Figure 12. Inverted stiffness coefficients of triclinic media. Dots indicate mean values, and bars correspond to the 95% confidence intervals resulting from adding Gaussian noise with the standard deviation equal to 12° for polarization vectors and 5% for the slownesses.

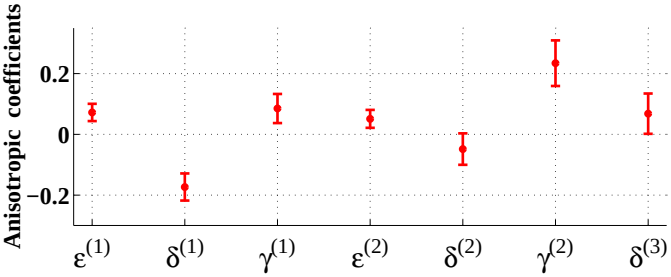

Figure 13. Tsvankin's (1997) anisotropic coefficients for the estimated orthorhombic media. As in Figure 12, dots indicate the mean values, and bars correspond to the 95% confidence intervals. The vertical velocities for the obtained models are $V_{P0} = 2.66 \pm 0.05$ km/s and $V_{S0} = 1.44 \pm 0.04$ km/s (not shown).

model correctly reproduces the direction of the S-wave polarization vectors at small offsets (Figures 11b, c) and the features displayed on the slowness plots (Figures 11d-f). In particular, the shear-wave splitting coefficient $\gamma^{(S)} = (\gamma^{(2)} - \gamma^{(1)})/(1 + 2\gamma^{(2)}) \approx 0.10$ corresponds to that inferred from Figures 11e, f. Also the elongation of the P-wave slowness contours in approximately the E-W direction (Figure 11d) corresponds to the inequality $\delta^{(2)} > \delta^{(1)}$ between two of the δ-coefficients [equation (20) in Grechka and Tsvankin (1999)].

Some insight into the goodness-of-fit of the data can be gained from the residuals $\Delta A^{(Q)}_i$ and $\Delta p^{(Q)}_3$ plotted in Figure 14. Our best-fit model is quite successful in predicting the S_1-wave slowness (Figure 14e), while the residuals of slownesses of P- and S_2-waves have some biases (Figures 14d, f). Likewise, the P-wave polarizations

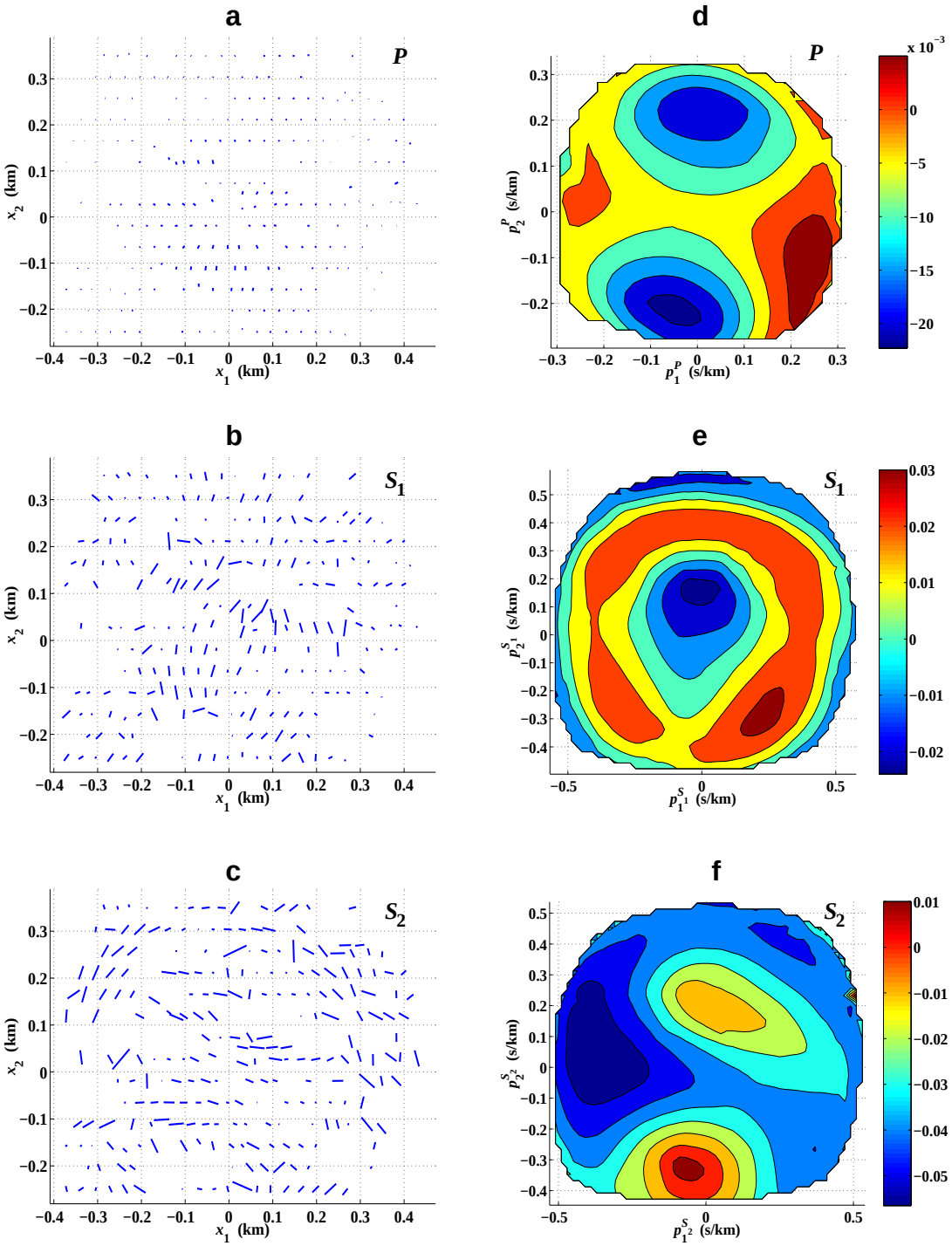

Figure 14. (a, b, c) Residuals of the horizontal components of the polarization vectors $\Delta A_i^{(Q)} = A_i^{(Q)\,\mathrm{meas}} - A_i^{(Q)\,\mathrm{comp}}$, $(i = 1, 2)$; (d, e, f) are the vertical slowness components $\Delta p_3^{(Q)} = p_3^{(Q)\,\mathrm{meas}} - p_3^{(Q)\,\mathrm{comp}}$ of the P-, S_1-, and S_2-waves. The computed quantities correspond to the triclinic model marked by dots in Figure 12. The scale for polarizations is the same as that in Figure 11.

(Figure 14a) are well described, whereas the polarizations of shear modes are relatively poor (Figures 14b, c). Since the residuals in Figures 14b, c,e and f display systematic patterns, it appears that errors in the inversion are mainly caused by the S-wave polarizations and slownesses. In fact, this observation could have been expected because the vectors $\boldsymbol{A}^{(S_1)}$ and $\boldsymbol{A}^{(S_2)}$ were obtained by applying Alford rotation, which implies the orthogonality $\boldsymbol{A}^{(S_1)} \perp \boldsymbol{A}^{(S_2)}$. At large incidence angles, however, the vectors $\boldsymbol{A}^{(S_1)}$ and $\boldsymbol{A}^{(S_2)}$ are not orthogonal to each other as can be verified from the corresponding slowness vectors $\boldsymbol{p}^{(S_1)}$ and $\boldsymbol{p}^{(S_2)}$ (Figures 11e, f), which are not parallel. This inconsistency propagates through the inversion scheme (which tries to fit all the data simultaneously) and contributes to the overall error.

Even given errors, our results agree with existing studies of the Vacuum Field. For instance, Mattocks (1998), who examined the polarization of S-waves and the focusing of shear-wave energy, concluded that the overburden (shallow 300 m) of the Vacuum Field has orthorhombic symmetry. In addition, the study of borehole breakouts performed by Scuta (1997) resulted in an estimate of azimuth of the maximum horizontal stress of about 32° SE. The η value predicted by the model is close to $\eta = 0.19$ obtained from nonhyperbolic moveout of surface P-wave data (Tsvankin, 2001).

Discussion and Conclusions

The feasibility of estimating the full stiffness tensor $\boldsymbol{c}$ from multi-component, multi-azimuth walkaway VSP data depends on several factors. First, the overburden complexity limits our ability to estimate the horizontal slowness components p_1 and p_2 at the geophone levels. When such estimates of p_1 and p_2 cannot be made (scenario 3), the problem is under-determined, rendering the inverted stiffnesses almost useless. We showed that knowing the horizontal slowness components of only P-waves (scenario 2) makes the inversion for all c_{ij} feasible. When the components of p_1 and p_2 of the shear-waves can be also measured (scenario 1), the stability of the inverted stiffness coefficients increases.

Another factor that governs the accuracy of any given c_{ij} is the data coverage. Since different stiffness coefficients influence wave propagation for different ranges of polar and azimuthal angles, full coverage may be needed to obtain all c_{ij} with a comparable accuracy. In practice, however, we can expect to have a much better coverage in near-vertical directions than near the horizontal. As a result, errors in c_{11}, c_{12}, c_{22}, and c_{66} are usually greater than those in c_{33}, c_{44}, and c_{55}. Our numerical tests confirm that.

In general, the accuracy of inverted stiffness coefficients increases if the medium has a known higher symmetry. This obviously relates to the number of unknown quantities one attempts to estimate from a given data set. We have found, though, that the gain in accuracy is not substantial enough to make the assumption of a particular symmetry absolutely necessary. On the other hand, allowing for the most general triclinic anisotropy offers the potential of recognizing the medium symmetry from the inversion results in contrast to assuming it *a priori*.

The presented case study substantiates this last point. We estimated the stiffness tensor of a triclinic model by fitting both the polarization and slowness vectors of the P- and two split S-waves. We also showed that the obtained stiffnesses are close to those describing an azimuthally rotated orthorhombic model. The orientation of its symmetry planes fits a number of independent observations and seems to relate to the subsurface stresses.

Acknowledgments

We are grateful to Ilya Tsvankin (CSM) for fruitful discussions, Ken Larner (CSM) for reviewing the manuscript and Tom Davis (with the Reservoir Characterization Project at CSM) for providing the data. P. Dewangan was supported by the members of the Consortium Project on Seismic Inverse Methods for Complex Structures at Center for Wave Phenomena, CSM. V. Grechka thanks Shell E&P for the permission to publish the paper.

REFERENCES

Alford, R. M., 1986, Shear data in the presence of azimuthal anisotropy: Ann. Internat. Mtg., Soc. Expl. Geophys., Expanded Abstracts, 476–479.

Bakulin, A., Grechka, V., and Tsvankin, I., 2000a, Estimation of fracture parameters from reflection seismic data. Part II: Fractured models with orthorhombic symmetry: Geophysics, **65**, 1803–1817.

Bakulin, A., Grechka, V., and Tsvankin, I., 2000b, Estimation of fracture parameters from reflection seismic data. Part III: Fractured models with monoclinic symmetry: Geophysics, **65**, 1818–1830.

Bakulin, A., Slater, C., Bunain, H., Grechka, V., 2000c, Estimation of azimuthal anisotropy and fracture parameters from multiazimuthal walkaway VSP in the presence of lateral heterogeneity: 70th Ann. Internat. Mtg., Soc. Expl. Geophys., Expanded Abstracts, 1405–1408.

Dellinger, J.A., Nolte, B., and Etgen, J.T., 2001, Alford rotation, ray theory, and crossed-dipole geometry: Geophysics, **66**, 637–647.

DiSiena, J.P., Gaiser, J.E., Corrigan, D., 1984, Horizontal components and shear wave analysis of three-component VSP data, *in* Toksoz, M.N., Steward, R.R., Eds., Vertical Seismic Profiling Part B: Advanced concepts, Handbook of geophysical exploration, Section I

(Seismic Exploration), **14b**, Geophysical Press, London, 177–188.

Gaiser, J.E., 1990, Transversely isotropic phase velocity analysis from slowness estimates: J. Geophys. Res., **95**, 241-254.

Grechka, V., Bakulin, A., and Tsvankin, I., 2001, Seismic characterization of vertical fractures described as general linear-slip interfaces: 63rd Conference of EAGE, Extended Abstracts, P-201.

Grechka, V., and Tsvankin, I., 1999, 3-D moveout velocity analysis and parameter estimation for orthorhombic media: Geophysics, **64**, 820–837.

Horne, S., and Leaney, S., 2000, Short note: Polarization and slowness component inversion for TI anisotropy: Geophys. Prosp., **48**, 779-788.

Mattocks, B., 1998, Borehole geophysical investigation of seismic anisotropy at Vacuum Field, Lea County, New Mexico: Ph.D. thesis, Colorado School of Mines.

Michaud, G., 2001, Multicomponent borehole seismic monitoring of a pilot CO_2 flood: Ph.D. thesis, Colorado School of Mines.

Miller, D.E., and Spencer, C., 1994, An exact inversion for anisotropic moduli from phase slowness data: J. Geophys. Res., **99**, 651-657.

Press, W.H., Flannery, B.P., Teukolsky, S.A., and Vetterling, W.T., 1987, Numerical recipes: the art of scientific computing: Cambridge University Press.

Roche, S., 1997, Time-lapse, multicomponent, three-dimensional seismic characterization of a San Andres shallow shelf carbonate reservoir, Vacuum Field, Lea County, New Mexico: Ph.D. thesis, Colorado School of Mines.

Sayers, C.M., 1997, Determination of anisotropic velocity models from walkaway VSP data acquired in the presence of dip: Geophysics, **62**, 723–729.

Scuta, M., 1997, 3-D Geological Characterization of Central Vacuum Unit, Lea County, New Mexico: Ph.D. thesis, Colorado School of Mines.

Tsvankin, I., 1997, Anisotropic parameters and P-wave velocity for orthorhombic media: Geophysics, **62**, 1292–1309.

Tsvankin, I., 2001, Seismic signatures and analysis of reflection data in anisotropic media: Pergamon, Amesterdam.